Parallel Dislocation Networks and Cottrell Atmospheres Reduce Thermal Conductivity of PbTe Thermoelectrics

Lamya Abdellaoui, Zhiwei Chen, Yuan Yu,* Ting Luo, Riley Hanus, Torsten Schwarz, Ruben Bueno Villoro, Oana Cojocaru-Mirédin, Gerald Jeffrey Snyder, Dierk Raabe, Yanzhong Pei, Christina Scheu,* and Siyuan Zhang*

Dislocations play an important role in thermal transport by scattering phonons. Nevertheless, for materials with intrinsically low thermal conductivity, such as thermoelectrics, classical models require exceedingly high numbers of dislocations ($>10^{12}$ cm^{-2}) to further impede thermal transport. In this work, a significant reduction in thermal conductivity of $Na_{0.025}Eu_{0.03}Pb_{0.945}Te$ is demonstrated at a moderate dislocation density of 1×10^{10} cm^{-2}. Further characteristics of dislocations, including their arrangement, orientation, and local chemistry are shown to be crucial to their phonon-scattering effect and are characterized by correlative microscopy techniques. Electron channeling contrast imaging reveals a uniform distribution of dislocations within individual grains, with parallel lines along four <111> directions. Transmission electron microscopy (TEM) shows the parallel networks are edge-type and share the same Burgers vectors within each group. Atom probe tomography reveals the enrichment of dopant Na at dislocation cores, forming Cottrell atmospheres. The dislocation network is demonstrated to be stable during in situ heating in the TEM. Using the Callaway transport model, it is demonstrated that both parallel arrangement of dislocations and Cottrell atmospheres make dislocations more efficient in phonon scattering. These two mechanisms provide new avenues to lower the thermal conductivity in materials for thermal-insulating applications.

1. Introduction

Thermoelectric materials provide a promising way to convert waste heat into electricity by the Seebeck effect.[1] The conversion efficiency is determined by the dimensionless figure of merit

$$zT = S^2\sigma T/\kappa \tag{1}$$

where S is the Seebeck coefficient, σ is the electrical conductivity, T is the absolute temperature, and κ is the thermal conductivity with contributions from the crystal lattice vibrations (κ_L) and the charge carriers (κ_e). Hence, a good thermoelectric material requires a large σ and S along with a low κ. As σ and S are closely interwoven, it is difficult to tune them individually. In addition, κ_e is proportional to σ via the Wiedemann–Franz law. Reducing κ_L is a relatively independent and effective approach to enhance zT. Efforts to reduce κ_L include introducing nano-scale inhomogeneities,[2] strong lattice anharmonicity,[3] materials with complex crystal structures,[4] and multi-scale structural defects to scatter phonons.[5]

Since the 1960s, PbTe alloys have been one of the leading commercial thermoelectric power generators for mid-temperature-range (600–800 K) applications, especially for space missions.[6] From the electronic transport perspective, the band structure of PbTe can be optimized by resonance state,[7] band convergence,[8] and band flattening,[9] all of which enhance the power factor $S^2\sigma$. From the thermal transport perspective, PbTe employs metavalent bonding,[10] which is the basis of the strong bond anharmonicity for the intrinsic phonon–phonon scattering

Dr. L. Abdellaoui, Dr. T. Luo, Dr. T. Schwarz, R. Bueno Villoro,
Prof. D. Raabe, Prof. C. Scheu, Dr. S. Zhang
Max-Planck-Institut für Eisenforschung GmbH
Max-Planck-Straße 1, 40237 Düsseldorf, Germany
E-mail: scheu@mpie.de; siyuan.zhang@mpie.de

Dr. Z. Chen, Prof. Y. Pei
Key Laboratory of Advanced Civil Engineering
Materials of Ministry of Education
School of Materials Science and Engineering
Tongji University
4800 Caoan Road, Shanghai 201804, China
Dr. Y. Yu, Dr. O. Cojocaru-Mirédin
Institute of Physics IA
RWTH Aachen University
52056 Aachen, Germany
E-mail: yu@physik.rwth-aachen.de
Dr. R. Hanus, Prof. G. J. Snyder
Department of Materials Science and Engineering
Northwestern University
Evanston 60208, USA

ADVANCED
SCIENCE NEWS
www.advancedsciencenews.com

ADVANCED
FUNCTIONAL
MATERIALS
www.afm-journal.de

and hence its intrinsically low κ_L. In addition, extrinsic phonon scattering processes by microstructural defects including point defects,[11] dislocations,[12] and interfaces,[2,13] have been successfully introduced to further lower the thermal conductivity.

In particular, dislocations have only recently been considered as a major contributor to phonon scattering and zT enhancement.[14] Although the mechanisms of dislocation scattering have been proposed for some time,[15] via the short range interactions at the dislocation core and long range interactions from dislocation strain, it had been assumed that these effects were relatively minor due to low dislocation density in materials of interest. Recently, however, there is increasing evidence that much of the phonon scattering observed in low thermal conductivity materials is actually due to dislocation scattering. For instance, interface or boundary scattering, long considered one of the most important scattering mechanism for thermoelectrics, actually has the T^2 temperature dependence in polycrystalline materials, predicted by dislocation scattering as opposed to the T^3 temperature dependence of a classical boundary.[16] Recent experiments show that dislocations can dominate scattering sufficient to engineer strong anisotropy of thermal conductivity in semiconductors.[17]

Recently, Chen et al., have reported high zT of p-type $Eu_{0.03}Na_{0.025}Pb_{0.945}Te$ thermoelectrics with ultralow κ_L values, reducing the intrinsically low κ_L of PbTe by half.[12c] The significant reduction was primarily attributed to the high density of dislocations, and their correlation to the strain field and lattice softening was later discussed.[12b,18] Nevertheless, to account for the observed thermal conductivity, a dislocation density exceeding 4×10^{12} cm^{-2} was proposed,[12c] corresponding to an average dislocation spacing of only 5 nm. Such dislocation networks can be present at semi-coherent interfaces, but they are difficult to maintain throughout the bulk of the materials. Such high density of dislocations is also prone to annihilation and rearrangement at elevated temperatures.

So far, most discussions on dislocations have treated them as individual scatterers and without a chemical identity. In this Article, we developed correlative microscopy techniques to study alignment of dislocation networks in $Eu_{0.03}Na_{0.025}Pb_{0.945}Te$ from the micrometer scale. All the way down to the atomic scale, we investigated the spatial extent and concentration profile of Cottrell atmospheres around dislocation cores by correlative aberration-corrected electron microscopy and atom probe tomography (APT). We found a moderate dislocation density, only $\approx 1 \times 10^{10}$ cm^{-2}, and demonstrated their stability at elevated temperatures. Our transport model shows both the parallel networks of dislocations and Cottrell atmospheres can significantly enhance phonon scattering. As a result, the experimentally observed low thermal conductivity is reached by only 0.25% of the dislocation density previously deemed necessary.[12c]

2. Results and Discussion

The distribution of dislocations on the micrometer scale is characterized using scanning electron microscopy (SEM). As shown in **Figure 1**a, most PbTe grains are equiaxed with an average grain size of 14.6 ± 0.8 μm. Black regions in Figure 1a observed at triple junctions between indexed PbTe grains are pores and

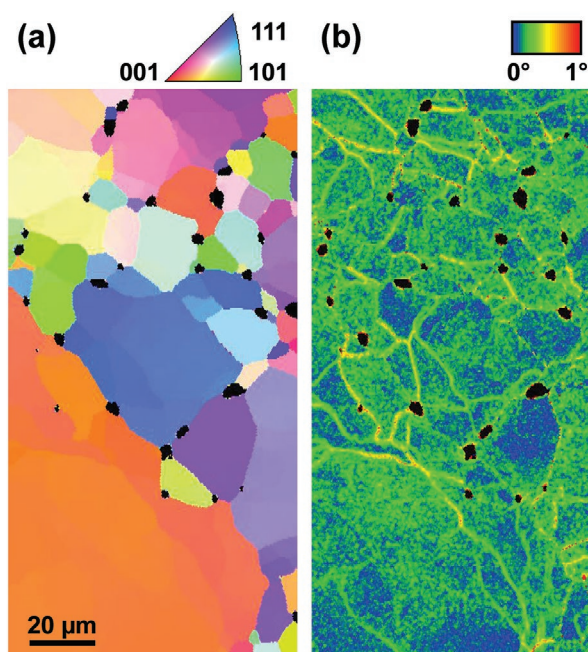**Figure 1.** Grain structure of $Eu_{0.03}Na_{0.025}Pb_{0.945}Te$ highlighting a) high angle grain boundaries in the electron back-scattered diffraction (EBSD) inverse pole figure map and b) misorientations caused by dislocation networks all over individual grains in the kernel average misorientation map.

precipitates enriched in Na and Eu, as identified by energy-dispersive X-ray spectroscopy (EDS) mapping in Figures S1 and S2, Supporting Information. Variations in individual PbTe grains are highlighted in the kernel average misorientation map (Figure 1b). It is evident that small misorientations (<1°) exist all across the individual grains. It is well known that an array of parallel dislocations will cause a misorientation θ depending on their Burgers vector b, and the average spacing d. The geometric relation is given by Equation (2):

$$2 \tan \frac{\theta}{2} = \frac{b}{d} \tag{2}$$

Taking $b = 0.457$ nm for PbTe, a 1° misorientation would correspond to an average spacing of 26 nm. For a dislocation density exceeding 4×10^{12} cm^{-2}, ($d < 5$ nm), the misorientation would be higher than 5°. From the observed misorientation in Figure 1b (<1°), we would expect geometrically necessary dislocation networks with much lower number density. To confirm this, we resort to imaging techniques to determine the density of dislocations, which can also account for dislocations that are not geometrically necessary.

The distribution of dislocations network within individual grains is investigated by electron channeling contrast imaging (ECCI)[19] in SEM. As shown in **Figure 2**a, the central grain is tilted to the channeling condition of $g = (\bar{2}00)$, and hence shows a darker contrast than the neighboring grains.[19] Networks of parallel line features are visible within the grain (Figure 2b). They are interpreted as dislocation lines, and the bright contrast stems from the disruption of the channeling condition by the strain field of the dislocations.[19] With the crystal orientation shown in Figure 2c, the dislocations can be
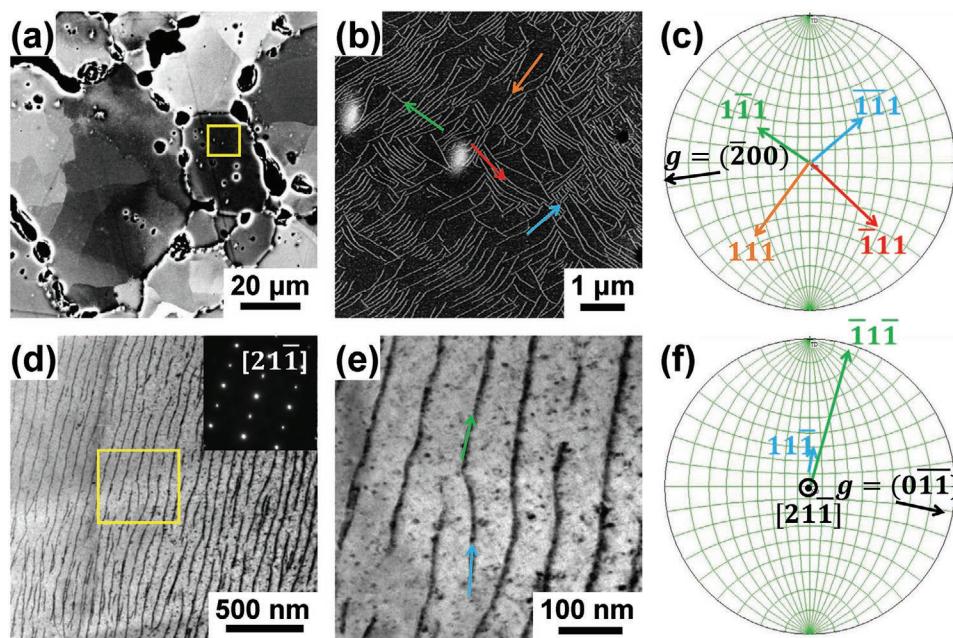
Figure 2. Correlative electron microscopy of dislocations in $Eu_{0.03}Na_{0.025}Pb_{0.945}Te$. a) ECCI image with the central grain (with the yellow box) tilted to the $g = (\bar{2}00)$ channeling condition. b) magnified region in the yellow box in (a) revealing four groups of dislocations along <111> directions. c) Stereographic projection of the grain orientation with highlighted <111> directions. d) BF image from a TEM lamella tilted to the $[21\bar{1}]$ zone axis presenting a high density of dislocations (inset: selected area diffraction pattern), e) magnified region from the yellow box in (d) presenting two sets of dislocations along $[11\bar{1}]$ and $[\bar{1}1\bar{1}]$ directions, as marked with blue and green arrows, respectively, as determined from f) the stereographic projection.

classified into 4 groups of parallel lines labelled by arrows in blue, green, red, and orange pointing to the dislocations lines in Figure 2b, corresponding to the $[\bar{1}\bar{1}1]$, $[\bar{1}1\bar{1}]$, $[\bar{1}111]$, and $[111]$ directions, respectively. This observation was reproduced in other grains (Figure S3): All dislocations have segments aligned to one of the 4 <111> directions.

Further characterization of the dislocation networks was performed using transmission electron microscopy (TEM). Individual dislocation cores in PbTe have been imaged confirming their Burgers vectors to be $\frac{1}{2}\langle 110 \rangle$-type.[12b,c] However, to confirm the Burgers vectors for entire sets of parallel dislocations, we employed weak beam dark field (WBDF) imaging under different diffraction conditions. The lamella presented in Figure 2d was tilted to the $[21\bar{1}]$ zone axis, and a high density of parallel dislocations are revealed in the bright field (BF) micrographs (Figure 2d,e). As shown in Figure S4, Supporting Information, the dislocations are composed of two line segments along $[11\bar{1}]$ and $[\bar{1}1\bar{1}]$ directions, with a number density of 3.7×10^9 and 6.5×10^9 cm^{-2}, respectively. Then, WBDF images confirm that each set has their distinct Burgers vector, $\frac{1}{2}[011]$ and $\frac{1}{2}[110]$, respectively, so that they are all edge dislocations (Table S1, Supporting Information).

Dislocations are known to introduce long-range strain fields around them.[12b,16a] Especially for edge-type dislocations, a dipole of tensile and compressive strain fields exist around their cores.[12b,15c] The strain field can attract dopants to segregate around dislocation cores, forming Cottrell atmospheres, which can further enhance phonon scattering.[5e,15b,20] Correlative TEM/APT measurements were performed to reveal segregation of dopants around dislocation cores.[21] **Figure 3**a shows the annular bright field (ABF) scanning transmission electron

microscopy (STEM) image of a needle-shaped APT specimen overlapped with the 3D reconstruction of APT results. Dislocations are highlighted by the iso-composition surfaces of 2 at% Na and indicated by arrows. Figure 3b displays the near-atomic-scale image of a dislocation as well as the distribution of Na in its vicinity. The dislocation line is straight, in agreement with the ECCI and TEM observations. Besides, a much higher concentration of Na atoms can be found around the dislocation cores. The aggregated Na atoms are not distributed homogeneously along the dislocation line but show some periodic enrichment which is akin to the Plateau–Rayleigh crystal growth.[21,22] These Na-decorated dislocations are further confirmed by additional APT measurements, as delineated by the 2 at% Na isosurfaces in Figure S5, Supporting Information. Figure 3c presents the composition profile as a function of distance from the dislocation core to the PbTe matrix. The composition of Na is 0.6 at% in the PbTe matrix and increases to 7 at% at the dislocation core within a distance of ≈2 nm around the dislocation core.

Correlating to the Na segregation around dislocation cores, we observed the depletion of Pb (Figure 3c). This suggests the formation of dislocations by the accumulation and collapse of Pb vacancies through activating Bardeen-Herring sources.[14a] Both Pb vacancies and the strain field of dislocations can attract Na atoms to form Cottrell atmosphere. The formation of Cottrell atmosphere in turn enhances the stability of dislocations by pinning their motion, an effect which further stabilizes the high density of dislocations.[23] It is worth noting Eu is not enriched at dislocation cores, likely due to the larger ionic radius of Eu and its slower diffusivity in PbTe than Na.[24] Na atoms are also found to segregate in nanoprecipitates with a
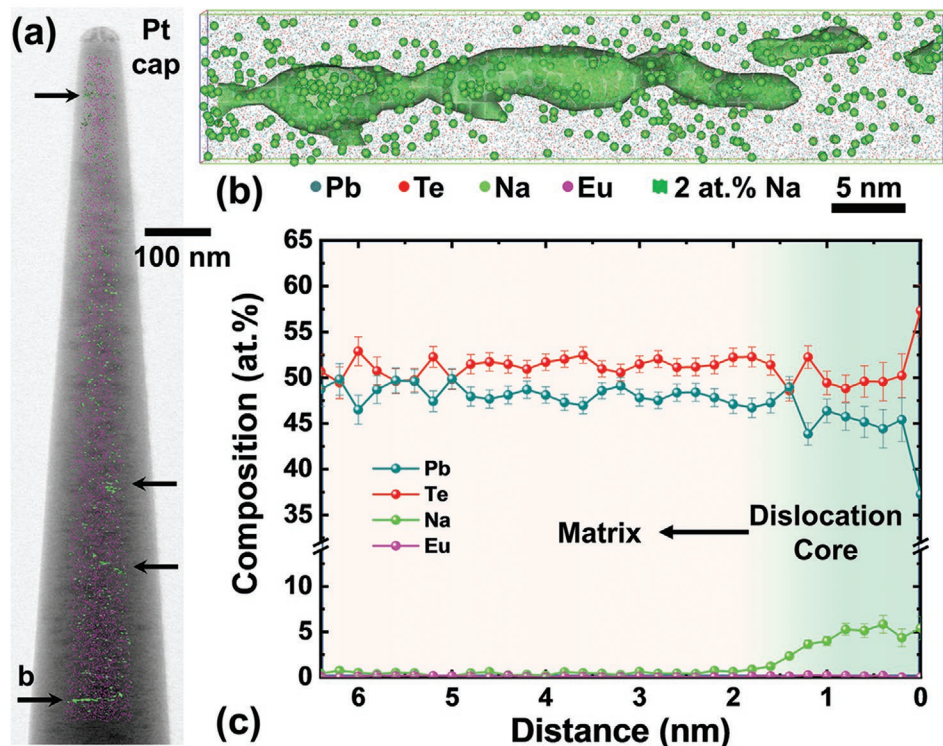
Figure 3. Atom probe tomography showing Na segregation to dislocation cores. a) ABF-STEM image of a needle-shaped APT specimen overlapped with the 3D APT reconstruction. Iso-composition surfaces of 2 at% Na are highlighted in green; linear defects (dislocations) are indicated by arrows. b) Magnified image of the bottom part in (a), showing the atomic distribution of Na in the vicinity of a dislocation. c) Composition proximity histogram taken from the Na iso-composition surface in (b), showing the formation of Na Cottrell atmosphere at a dislocation core.

high number density of 5×10^{23} cm^{-3} and small size (5 nm in diameter) in the alloy, which is further discussed in the supplementary information (Figures S6 and S7, Supporting Information). Only one small Eu-rich precipitate was occasionally found by APT (Figure S8, Supporting Information), and their number density is hence negligible.

To validate the thermal stability of the dislocation networks, in situ heating experiments were conducted in the TEM. As shown in Videos S1 and S2, and their excerpts in Figure S9, Supporting Information, the dislocation network is stable during in situ heating from room temperature to 523 K. Higher annealing temperatures were prohibited by excessive sublimation of PbTe into the TEM vacuum. During the fast ramp up and quenching at 3 K s^{-1}, as well as isothermal annealing for over 10 min, individual dislocations within the network did not show any motion from their starting positions.

Although dislocations, unlike vacancies, are non-equilibrium defects, the observed networks have dislocations so far apart (100 nm on average) that they remain stable for a wide temperature range. As discussed, the observed Cottrell atmosphere can further hinder the motion of dislocations. The observed arrangement of dislocation networks was likely stabilized at high temperatures during multiple annealing steps. The stable configuration of the dislocation networks and hence their number density suggest that they can contribute to phonon scattering over a wide temperature range.

In the following, we analyze the effect of the parallel alignment of dislocation networks and the presence of Cottrell

atmospheres on the lattice thermal conductivity. A Callaway-type model is applied to model the lattice thermal conductivity (Equation (3)), using the Born-von Karman dispersion as described by Chen et al.[25]

$$\kappa_L = \frac{k_B}{2\pi^2} \left(\frac{k_B T}{\hbar} \right)^3 \int_0^{\Theta_D/T} \frac{v_g}{v_p^2} \tau_{tot}(x) \frac{x^4 e^x}{(e^x - 1)^2} dx \qquad (3)$$

where v_g and v_p are the group and phase velocities of phonons, k_B is the Boltzmann constant, T is the absolute temperature, Θ_D is the acoustic Debye temperature, τ_{tot} is the total relaxation time and

$$x = \hbar\omega/k_B T \qquad (4)$$

with ω the phonon angular frequency and $\hbar$ the reduced Planck constant. The total relaxation time τ_{tot} (Equation (5)) includes contributions from various scattering processes according to the Matthiessen's rule:

$$\tau_{tot}^{-1} = \sum_i \tau_i^{-1} \qquad (5)$$

The individual terms τ_i^{-1} and their analytical expressions are listed in Table S2, Supporting Information, and values for all the parameters are listed in Table S3, Supporting Information. In particular, the Umklapp process (τ_U^{-1}) and dislocations play the dominant roles in phonon scattering. Dislocations
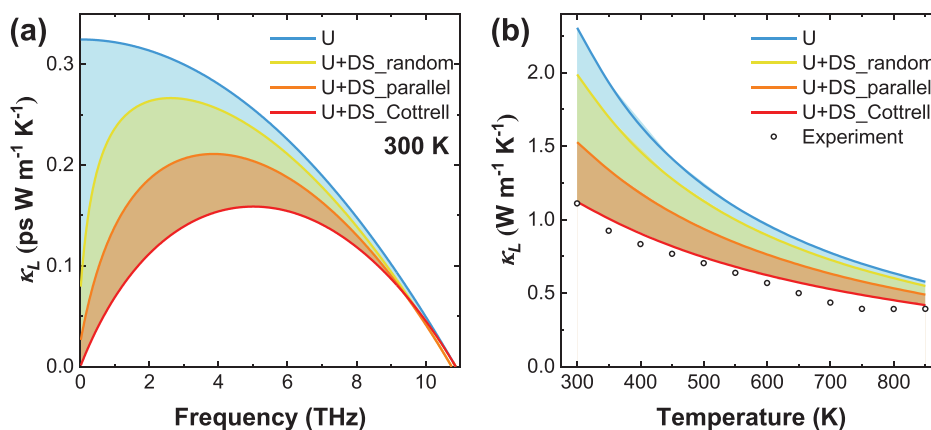
**ADVANCED
SCIENCE NEWS**

www.advancedsciencenews.com

**ADVANCED
FUNCTIONAL
MATERIALS**

www.afm-journal.de

Figure 4. Thermal conductivity impacted by dislocations. a) The calculated spectral lattice thermal conductivity (κ_L) at 300 K and b) temperature dependence of κ_L using the modelled scattering terms from the Umklapp process (U) and dislocation strain field (DS) comparing random versus parallel dislocation arrangements and the effect of the Cottrell atmosphere. The experimental κ_L values[25] are plotted as a reference.

scatter phonons through the composition fluctuation around the core (τ_{DC}^{-1}) as well as the strain field (τ_{DS}^{-1}). Due to its long-range nature, the dislocation strain field scatters phonons much more strongly than the cores. For $Na_{0.025}Eu_{0.03}Pb_{0.945}Te$, the limited scattering strength of the dislocation core term is shown in Figure S10, Supporting Information. Likewise, scattering from the solid solutions of Na and Eu, at their respective concentration 0.6% and 0.55%, have a negligible effect in phonon scattering.

The scattering strength of dislocation strain fields scales linearly with the phonon frequency ω. In our observed microstructure of $Na_{0.025}Eu_{0.03}Pb_{0.945}Te$, dislocations form networks, and hence it is worth discussing the diffraction and dimensionality crossover effects.[26] At the observed dislocation spacing of the network, ≈100 nm, the crossover frequency (0.07 THz) is well below the Debye frequency (11 THz), so that we can safely apply the linear scaling of ω for the whole frequency range.

Klemens has laid the foundation to formulate the scattering term of dislocation strain fields.[15a] Carruthers then took the long range nature of the strain field into consideration, proposing the formula in Equation (6):[15c]

$$\tau_{DS}^{-1} = \beta\gamma^2\omega N_D b^2, \text{ with } \beta = \frac{1}{3}\left(\ln\frac{l}{b}\right)^2 \quad (6)$$

where γ is the Grüneisen parameter, N_D is the dislocation density, l is the range of the strain field, and β is a term quantifying the long-range effect of the strain field. The model has been proposed to explain the significant reduction of thermal conductivity in LiF,[15c] and recently applied to model the threading dislocation networks in GaN films.[27]

As discussed above, dislocations in $Na_{0.025}Eu_{0.03}Pb_{0.945}Te$ are aligned along 4 types of <111> directions and constitute the parallel networks. We model their effect by considering 2 groups of dislocations, each having a number density of 5×10^9 cm^{-2}, as an average from the number density determined by TEM. The total number of dislocations which contribute to the scattering rate is therefore $N_D = 1 \times 10^{10}$ cm^{-2}. If we assume the dislocations are randomly oriented, a good treatment is $l = d$, where $d = 100$ nm is the average dislocation spacing, giving $\beta = 9.7$. For

the observed network, dislocations in each group are aligned in parallel. If we assume that none of the dislocations within a grain interfere as a maximum scattering approximation, a good treatment is $l = D$, where $D = 15$ μm is the grain size. This is equivalent to describing the resulting strain field of ≈100 parallel dislocations with the same Burgers vector, lying on the same slip plane, giving $\beta = 36$. In the original treatment, Carruthers suggested the consideration of 30 to 1000 parallel dislocations.[15c]

The effect of the parallel arrangement of dislocations on phonon scattering is compared in **Figure 4**. In addition to the Umklapp scattering plotted with respect to phonon frequency (Figure 4a) and temperature (Figure 4b), scattering by dislocation strain fields further reduce κ_L by the shaded areas in cyan color. As the parallel arrangement is taken into consideration, the shaded areas in yellow shows a further reduction of κ_L.

Next, we consider the effect of Na segregation around dislocations on the rate of phonon scattering. The influence of Cottrell atmospheres on phonon-dislocation scattering can be modeled by modifying the Grüneisen parameter.[15b,20c] Due to the large mismatches in the size and mass between Na and Pb (Equations (7) and (8)), the resulting modified Grüneisen parameter γ_D would be 2.61 according to Equation (9), where B is the bulk modulus, V_0 is the atomic volume, and c_0 is the Na concentration in solid solution.

$$\Delta m = -\frac{1}{2}\frac{m_{Na} - m_{Pb}}{m_{Pb}} = 0.44 \quad (7)$$

$$\Delta V = \frac{V_{Na} - V_{Pb}}{V_{Pb}} = -0.37 \quad (8)$$

$$\gamma_D = \gamma + \frac{BV_0c_0}{k_BT}\Delta V(\gamma\Delta V - \Delta m) = 2.61 \quad (9)$$

Substituting γ by γ_D into Equation (6), the scattering term is further enhanced by a factor of $(\gamma_D/\gamma)^2$, which is estimated to be 2.5. The κ_L reduction by the presence of Cottrell atmosphere around the dislocations is highlighted by the orange shading in Figure 4. It was found that Cottrell atmospheres strongly

strengthen the dislocation strain field phonon scattering but have a very limited effect on the dislocation core scattering term (Figure S10, Supporting Information).

As we demonstrate, phonon dislocation scattering has a strong effect in PbTe, and can be magnified further by engineering the alignment of dislocations and the composition near the core. It is evident that dislocations provide the most dominant phonon scattering effect. The stability of the dislocation network makes the κ_L reduction also effective at higher temperatures. At elevated temperatures, phonon–phonon scattering begins to dominate making lattice softening, or the reduction of phonon energy and group velocity, an important effect to quantify.[18] The phonon velocities used in our model are listed in Table S4, Supporting Information, which are calculated based on the temperature-dependent elastic moduli of PbTe.[28]

3. Conclusions

In summary, we thoroughly examined the microstructural features in a $Eu_{0.03}Na_{0.025}Pb_{0.945}Te$ thermoelectric material with very low lattice thermal conductivity. Structural characterization from the grain size length scale (15 µm) down to the atomic scale is bridged by correlating electron backscattering diffraction (EBSD), ECCI, TEM, and APT measurements from the same area. We found that dislocations are uniformly present throughout the alloy and they contribute most to κ_L reduction. In particular, these dislocations form sets of parallel networks, each aligned parallel to one of the four <111> directions. Pb vacancies and Na dopants segregate around dislocation cores to form Cottrell atmospheres, providing pinning effects to dislocation motion. From in situ heating observations, the dislocation network does not show motion during heating up, quenching down, or isothermal annealing. Based on the quantification of the distribution, number density, size, and composition of the microstructural defects, their contributions to phonon scattering are evaluated using the Callaway model. The parallel alignment of dislocations and the Na Cottrell atmospheres enhance the scattering strength of their strain field, and they account for significant κ_L reduction with a moderate number density of 1×10^{10} cm^{-2}. We highlight the importance of understanding not only the structural and chemical characteristics of the property-defining defects, but also their large-scale alignment. The demonstrated correlative microscopy method bridges multiple length scales and is a powerful tool to correlate complex microstructures to the properties of functional materials.

4. Experimental Section

The alloy of $Eu_{0.03}Na_{0.025}Pb_{0.945}Te$ was synthesized by melting the stoichiometric amount of high purity elements at 1273 K for 6 h, and then quenched in cold water. To stabilize the microstructure and the thermoelectric properties, samples were annealed at 950 K for 3 days. The obtained ingot was later grinded into powders, and then hot pressed at 673 K under uniaxial pressure of 90 MPa for 20 min. The obtained pellet had a diameter of 12 mm and a thickness of 2 mm. Further information can be found in ref. [12c]

Samples for SEM were first grinded and polished using SiC papers and OPS+H_2O_2 solution, respectively. Afterward, the sample surface was polished by Ar ions using a Gatan Model 682 PECS operated at 2–3 kV.

EBSD mapping was performed using a JEOL-JSM-6490 microscope equipped with an EDAX/TSL EBSD system and a Digiview IV camera. The microscope was operated at 15 kV with a current of 2 nA. The sample had a working distance of 23 mm from the detector, and the scan was performed at a step size of 0.5 µm. ECCI was performed on a Zeiss Merlin FE-SEM microscope, operated at 30 kV, a working distance of 7–8 mm and a current of 2–4 nA. To orient the sample toward 2-beam diffraction conditions for controlled ECCI imaging, tilting of the SEM stage was guided by the computer program TOCA.[19] EDS spectrum imaging was performed on the same SEM operated at 25 kV, a working distance of 10 mm, a beam current of 2 nA, and recorded using a Bruker XFlash 6 detector.

Samples for TEM and STEM were prepared using a Scios2 focused ion beam (FIB). TEM and STEM imaging was conducted using a Titan Themis microscope operated at 300 kV. STEM micrographs were taken by high-angle annular dark field (HAADF), low-angle annular dark field (LAADF) and ABF detectors, with collection semi-angles of 73–200, 17–73, and 8–16 mrad, respectively. EDS spectrum imaging was performed using the FEI super-X detector. Multivariate statistical analysis[29] was carried out to enhance signal over noise and facilitate elemental quantification. In situ heating experiments were conducted on FIB lamella welded on heating chips from DENSsolutions (See Figure S9a,b, Supporting Information). Individual HAADF, LAADF, ABF-STEM images were taken at ≈3 s intervals and correlated to the heating history to assign the temperatures to individual frames.

A correlative ECCI-STEM-APT study was conducted in this work. Accordingly, the APT specimens were prepared from the same grain that has been analyzed by ECCI using the Helios Nanolab 600i SEM. A standard FIB lift-out method was used to prepare the needle-shaped specimen with a low-voltage (5 kV) cleaning process at the final step to remove the surface Ga-ion implantation. The needle-shaped specimens were mounted on a half-Mo grid to accommodate both TEM and APT sample stages. After STEM imaging, the APT measurement was carried out on a Cameca LEAP 4000X Si. The laser pulses were adapted with a wavelength of 355 nm, a pulse duration of 10 ps and a pulse energy of 25 pJ. A pulse repetition rate of 200 kHz with a detection rate of 1% on average, an ion flight path of 160 mm, and a specimen base temperature of 40 K were utilized.

More APT measurements were conducted with a Cameca LEAP 5000 XR, using a laser pulse energy of 8 pJ, a detection rate of 0.6%, a laser pulse frequency of 100 kHz, and a base temperature of 35 K. Different APT experimental parameters were chosen for two different equipment to assure the best data-collection condition. The data reconstruction was performed on the Imago visualization and analysis system 3.8.2 and 3.8.4 from Cameca instruments.

Supporting Information

Supporting Information is available from the Wiley Online Library or from the author.

Acknowledgements

Conflict of Interest

The authors declare no conflict of interest.

Data Availability Statement

Data available in article supplementary material.

Keywords

[1] a) X.-L. Shi, J. Zou, Z.-G. Chen, *Chem. Rev.* **2020**, *120*, 7399; b) G. J. Snyder, E. S. Toberer, *Nat. Mater.* **2008**, *7*, 105; c) G. Tan, L. D. Zhao, M. G. Kanatzidis, *Chem. Rev.* **2016**, *116*, 12123; d) T. Zhu, Y. Liu, C. Fu, J. P. Heremans, G. J. Snyder, X. Zhao, *Adv. Mater.* **2017**, *29*, 1605884; e) J. He, T. M. Tritt, *Science* **2017**, *357*, eaak9997.

[2] K. F. Hsu, S. Loo, F. Guo, W. Chen, J. S. Dyck, C. Uher, T. Hogan, E. K. Polychroniadis, M. G. Kanatzidis, *Science* **2004**, *303*, 818.

[3] a) L. D. Zhao, S. H. Lo, Y. Zhang, H. Sun, G. Tan, C. Uher, C. Wolverton, V. P. Dravid, M. G. Kanatzidis, *Nature* **2014**, *508*, 373; b) J. P. Heremans, *Nat. Phys.* **2015**, *11*, 990; c) O. Delaire, J. Ma, K. Marty, A. F. May, M. A. McGuire, M. H. Du, D. J. Singh, A. Podlesnyak, G. Ehlers, M. D. Lumsden, B. C. Sales, *Nat. Mater.* **2011**, *10*, 614.

[4] a) S. Lin, W. Li, S. Li, X. Zhang, Z. Chen, Y. Xu, Y. Chen, Y. Pei, *Joule* **2017**, *1*, 816; b) K. Kurosaki, S. Yamanaka, *Phys. Status Solidi A* **2013**, *210*, 82.

[5] a) S. Wang, Y. Xiao, Y. Chen, S. Peng, D. Wang, T. Hong, Z. Yang, Y. Sun, X. Gao, L.-D. Zhao, *Energy Environ. Sci.* **2021**, *14*, 451; b) K. Biswas, J. He, I. D. Blum, C. I. Wu, T. P. Hogan, D. N. Seidman, V. P. Dravid, M. G. Kanatzidis, *Nature* **2012**, *489*, 414; c) L.-D. Zhao, V. P. Dravid, M. G. Kanatzidis, *Energy Environ. Sci.* **2014**, *7*, 251; d) X. Zhou, Y. Yan, X. Lu, H. Zhu, X. Han, G. Chen, Z. Ren, *Mater. Today* **2018**, *21*, 974; e) Y. Yu, C. Zhou, S. Zhang, M. Zhu, M. Wuttig, C. Scheu, D. Raabe, G. J. Snyder, B. Gault, O. Cojocaru-Mirédin, *Mater. Today* **2020**, *32*, 260.

[6] A. D. LaLonde, Y. Pei, H. Wang, G. J. Snyder, *Mater. Today* **2011**, *14*, 526.

[7] J. P. Heremans, V. Jovovic, E. S. Toberer, A. Saramat, K. Kurosaki, A. Charoenphakdee, S. Yamanaka, G. J. Snyder, *Science* **2008**, *321*, 554.

[8] a) Y. Pei, X. Shi, A. LaLonde, H. Wang, L. Chen, G. J. Snyder, *Nature* **2011**, *473*, 66; b) J. Zhang, R. Liu, N. Cheng, Y. Zhang, J. Yang, C. Uher, X. Shi, L. Chen, W. Zhang, *Adv. Mater.* **2014**, *26*, 3848.

[9] a) X. Qian, H. Wu, D. Wang, Y. Zhang, J. Wang, G. Wang, L. Zheng, S. J. Pennycook, L.-D. Zhao, *Energy Environ. Sci.* **2019**, *12*, 1969; b) C. Zhou, Y. Yu, Y. K. Lee, O. Cojocaru-Mirédin, B. Yoo, S.-P. Cho, J. Im, M. Wuttig, T. Hyeon, I. Chung, *J. Am. Chem. Soc.* **2018**, *140*, 15535.

[10] a) Y. Yu, M. Cagnoni, O. Cojocaru-Mirédin, M. Wuttig, *Adv. Funct. Mater.* **2020**, *30*, 1904862; b) S. Lee, K. Esfarjani, T. Luo, J. Zhou, Z. Tian, G. Chen, *Nat. Commun.* **2014**, *5*, 3525.

[11] L. Fu, M. Yin, D. Wu, W. Li, D. Feng, L. Huang, J. He, *Energy Environ. Sci.* **2017**, *10*, 2030.

[12] a) P.-Y. Deng, K.-K. Wang, J.-Y. Du, H.-J. Wu, *Adv. Funct. Mater.* **2020**, *30*, 2005479; b) Y. Wu, Z. Chen, P. Nan, F. Xiong, S. Lin, X. Zhang, Y. Chen, L. Chen, B. Ge, Y. Pei, *Joule* **2019**, *3*, 1276; c) Z. Chen, Z. Jian, W. Li, Y. Chang, B. Ge, R. Hanus, J. Yang, Y. Chen, M. Huang, G. J. Snyder, Y. Pei, *Adv. Mater.* **2017**, *29*, 1606768; d) Y. Sun, Y. Zhou, J. Han, W. Liu, C. Nan, M. Lin, M. Hu, B. Xu, *npj Comput. Mater.* **2019**, *5*, 97.

[13] a) K. Biswas, J. He, Q. Zhang, G. Wang, C. Uher, V. P. Dravid, M. G. Kanatzidis, *Nat. Chem.* **2011**, *3*, 160; b) S. Liu, Y. Yu, D. Wu, X. Xu, L. Xie, X. Chao, M. Bosman, S. J. Pennycook, Z. Yang, J. He, *Adv. Funct. Mater.* **2021**, *31*, 2007340; c) B. Xiang, J. Liu, J. Yan, M. Xia, Q. Zhang, L. Chen, J. Li, X. Y. Tan, Q. Yan, Y. Wu, *J. Mater. Chem. A* **2019**, *7*, 18458; d) J. He, S. N. Girard, M. G. Kanatzidis, V. P. Dravid, *Adv. Funct. Mater.* **2010**, *20*, 764.

[14] a) Z. Chen, B. Ge, W. Li, S. Lin, J. Shen, Y. Chang, R. Hanus, G. J. Snyder, Y. Pei, *Nat. Commun.* **2017**, *8*, 13828; b) S. I. Kim, K. H. Lee, H. A. Mun, H. S. Kim, S. W. Hwang, J. W. Roh, D. J. Yang, W. H. Shin, X. S. Li, Y. H. Lee, *Science* **2015**, *348*, 109; c) M. Hong, Z.-G. Chen, S. Matsumura, J. Zou, *Nano Energy* **2018**, *50*, 785.

[15] a) P. G. Klemens, *Proc. Phys. Soc., Sect. A* **1955**, *68*, 1113; b) P. G. Klemens, *J. Appl. Phys.* **1968**, *39*, 5304; c) P. Carruthers, *Phys. Rev.* **1959**, *114*, 995.

[16] a) H.-S. Kim, S. D. Kang, Y. Tang, R. Hanus, G. J. Snyder, *Mater. Horiz.* **2016**, *3*, 234; b) H.-S. Kim, S. I. Kim, K. H. Lee, S. W. Kim, G. J. Snyder, *Phys. Status Solidi B* **2017**, *254*, 1600103.

[17] B. Sun, G. Haunschild, C. Polanco, J. Ju, L. Lindsay, G. Koblmüller, Y. K. Koh, *Nat. Mater.* **2019**, *18*, 136.

[18] R. Hanus, M. T. Agne, A. J. E. Rettie, Z. Chen, G. Tan, D. Y. Chung, M. G. Kanatzidis, Y. Pei, P. W. Voorhees, G. J. Snyder, *Adv. Mater.* **2019**, *31*, 1900108.

[19] S. Zaefferer, N.-N. Elhami, *Acta Mater.* **2014**, *75*, 20.

[20] a) Y. Yu, S. Zhang, A. M. Mio, B. Gault, A. Sheskin, C. Scheu, D. Raabe, F. Zu, M. Wuttig, Y. Amouyal, O. Cojocaru-Miredin, *ACS Appl. Mater. Interfaces* **2018**, *10*, 3609; b) S. Giaremis, J. Kioseoglou, P. Desmarchelier, A. Tanguy, M. Isaiev, I. Belabbas, P. Kominou, K. Termentzidis, *ACS Appl. Energy Mater.* **2020**, *3*, 2682; c) M. W. Ackerman, P. G. Klemens, *J. Appl. Phys.* **1971**, *42*, 968.

[21] M. Kuzmina, M. Herbig, D. Ponge, S. Sandlobes, D. Raabe, *Science* **2015**, *349*, 1080.

[22] R. W. Day, M. N. Mankin, R. Gao, Y. S. No, S. K. Kim, D. C. Bell, H. G. Park, C. M. Lieber, *Nat. Nanotechnol.* **2015**, *10*, 345.

[23] K. Thompson, P. L. Flaitz, P. Ronsheim, D. J. Larson, T. F. Kelly, *Science* **2007**, *317*, 1370.

[24] X. Wang, I. Veremchuk, U. Burkhardt, M. Bobnar, H. Böttner, C.-Y. Kuo, C.-T. Chen, C.-F. Chang, J.-T. Zhao, Y. Grin, *J. Mater. Chem. C* **2018**, *6*, 9482.

[25] Z. Chen, X. Zhang, S. Lin, L. Chen, Y. Pei, *Natl. Sci. Rev.* **2018**, *5*, 888.

[26] R. Hanus, A. Garg, G. J. Snyder, *Commun. Phys.* **2018**, *1*, 78.

[27] H. Li, R. Hanus, C. A. Polanco, A. Zeidler, G. Koblmüller, Y. K. Koh, L. Lindsay, *Phys. Rev. B* **2020**, *102*, 014313.

[28] F. Ren, E. D. Case, J. R. Sootsman, M. G. Kanatzidis, H. Kong, C. Uher, E. Lara-Curzio, R. M. Trejo, *Acta Mater.* **2008**, *56*, 5954.

[29] S. Zhang, C. Scheu, *Microscopy* **2018**, *67*, i133.